

# Mutual induction of magnetic $3d$ and $4f$ order in multiferroic hexagonal $\text{ErMnO}_3$

D. Meier,<sup>1,2,\*</sup> H. Ryll,<sup>3</sup> K. Kiefer,<sup>3</sup> B. Klemke,<sup>3</sup> J.-U. Hoffmann,<sup>3</sup> R. Ramesh,<sup>1,2,4</sup> and M. Fiebig<sup>5</sup>

<sup>1</sup>Department of Materials Science and Engineering, University of California, Berkeley, CA 94720, USA

<sup>2</sup>Department of Physics, University of California, Berkeley, CA 94720, USA

<sup>3</sup>Helmholtz-Zentrum Berlin für Materialien und Energie, 14109 Berlin, Germany

<sup>4</sup>Materials Science Division, Lawrence Berkeley National Laboratory, Berkeley, CA 94720, USA and

<sup>5</sup>Department of Materials, ETH Zurich, 8093 Zurich, Switzerland

(Dated: November 5, 2018)

The complex interplay between the  $3d$  and  $4f$  moments in hexagonal  $\text{ErMnO}_3$  is investigated by magnetization, optical second harmonic generation, and neutron-diffraction measurements. We revise the phase diagram and provide a microscopic model for the emergent spin structures with a special focus on the intermediary phase transitions. Our measurements reveal that the  $3d$  exchange between  $\text{Mn}^{3+}$  ions dominates the magnetic symmetry at  $10 \text{ K} < T < T_N$  with  $\text{Mn}^{3+}$  order according to the  $\Gamma_4$  representation triggering  $4f$  ordering according to the same representation on the  $\text{Er}^{3+}(4b)$  site. Below  $10 \text{ K}$  the magnetic order is governed by  $4f$  exchange interactions of  $\text{Er}^{3+}$  ions on the  $2a$  site. The magnetic  $\text{Er}^{3+}(2a)$  order according to the representation  $\Gamma_2$  induces a magnetic reorientation ( $\Gamma_4 \rightarrow \Gamma_2$ ) at the  $\text{Er}^{3+}(4b)$  and the  $\text{Mn}^{3+}$  sites. Our findings highlight the fundamentally different roles the  $\text{Mn}^{3+}$ ,  $R^{3+}(2a)$ , and  $R^{3+}(4b)$  magnetism play in establishing the magnetic phase diagram of the hexagonal  $\text{RMnO}_3$  system.

## I. INTRODUCTION: MULTIFERROIC HEXAGONAL MANGANITES

Materials with coexisting magnetic and electric order, the so-called multiferroics, have been attracting a lot of attention since it was recognized that they can display gigantic magnetoelectric coupling effects: Magnetic properties can be controlled by electric fields and vice versa.<sup>2–5</sup> In this context the hexagonal (h-) manganites  $\text{h-RMnO}_3$  with  $R = \text{Sc, Y, Dy-Lu}$  play an exceptional role because they offer great flexibility for tuning such magnetoelectric correlations and studying the coupling between spin, charge, and lattice degrees of freedom in multiferroics. Crystals of the  $\text{h-RMnO}_3$  family are structurally equivalent and display ferroelectric order below about  $1000 \text{ K}$  with a spontaneous polarization of  $\approx 5.6 \mu\text{C}/\text{cm}^2$  along the hexagonal  $c$ -axis.<sup>6–8</sup> The  $R^{3+}$  ions vary in size and magnetic moment and due to the interaction with the  $\text{Mn}^{3+}$  ions the variety of magnetic phases and magnetoelectric interaction phenomena emerging below about  $100 \text{ K}$  is particularly rich. This includes contributions to the magnetization induced by ferroelectric poling, giant magneto-elastic coupling effects, and a coupling between magnetic and ferroelectric domain walls.<sup>9–11</sup>

A discussion of the magnetoelectric coupling phenomena in the  $\text{h-RMnO}_3$  compounds with  $R = \text{Dy-Yb}$  invariably involves the magnetic  $4f$  moments. Yet, investigations of the rare-earth order had remained scarce for a long time. Only recently, earlier magnetization measurements have been complemented by a structural analysis of the  $R^{3+}$  order in  $\text{h-HoMnO}_3$ ,  $\text{h-YbMnO}_3$ , and  $\text{h-DyMnO}_3$  by neutron or resonant x-ray diffraction. The studies revealed that the  $3d$ – $4f$  interaction in  $\text{h-RMnO}_3$  is more complex than previously assumed<sup>12–17</sup> and that the magnetic  $\text{Mn}^{3+}$  and  $R^{3+}$  lattices can have a different space symmetry.<sup>18</sup> Yet, with very few exceptions<sup>12</sup> little is known about the  $4f$ – $4f$  exchange interaction between  $R^{3+}$  moments occupying different Wyckoff positions, i.e., the  $4b$  and  $2a$  sites of the hexagonal unit

cell (see inset of Fig. 3 (a) for a schematic illustration). A detailed knowledge, however, is indispensable for understanding the complex magnetic, multiferroic, and magnetoelectric coupling processes in  $\text{h-RMnO}_3$ . It becomes even more important in view of the current intensive studies addressing the domain walls<sup>19–22</sup> and their magnetic properties.<sup>23</sup> Here, any statement about the *local* magnetic properties initially requires a precise knowledge of the *global* bulk spin structure. Consequently, the first goal is to develop a model explaining the magnetic phase diagram of the  $\text{h-RMnO}_3$  series in general.

For our study we have chosen  $\text{h-ErMnO}_3$  — its magnetic  $\text{Mn}^{3+}$  phase diagram is similar to that of  $\text{h-TmMnO}_3$  and  $\text{h-YbMnO}_3$  which establishes it as a prototypical compound within the  $\text{h-RMnO}_3$  series. Based on magnetoelectric and magnetization measurements a magnetic  $\text{Er}^{3+}$  order was proposed<sup>15,24</sup> but not verified or uniquely related to the coexisting  $\text{Mn}^{3+}$  order.

In this Report we clarify the spin structure of the  $\text{Mn}^{3+}$  and  $\text{Er}^{3+}$  sublattices and introduce a microscopic model coherently explaining the magnetic phase diagram of  $\text{h-ErMnO}_3$  that can be projected onto the  $\text{h-RMnO}_3$  system in general. For this purpose we performed complementary magnetization, second harmonic generation (SHG), and neutron-diffraction measurements at temperatures down to  $30 \text{ mK}$ . Below the Néel temperature we find antiferromagnetic order of the  $\text{Mn}^{3+}$  moments triggering the magnetic order of the  $\text{Er}^{3+}(4b)$  site according to the same representation ( $\Gamma_4^{\text{Er,Mn}}$ ) while the  $\text{Er}^{3+}(2a)$  sites remain disordered. In contrast, the ground state toward  $0 \text{ K}$  is ferrimagnetic with *all* spins ordered according to the same representation ( $\Gamma_2^{\text{Er,Mn}}$ ). The intermediary phase transition ( $\Gamma_4^{\text{Er,Mn}} \rightarrow \Gamma_2^{\text{Er,Mn}}$ ) occurs via a transient breakdown of the magnetic order on the  $\text{Mn}^{3+}$  and  $\text{Er}^{3+}(4b)$  sites so that the highest possible symmetry is maintained. The study advances our understanding of the different roles the  $\text{Mn}^{3+}$ ,  $R^{3+}(2a)$ , and  $R^{3+}(4b)$  moments play in establishing the magnetic phase diagram of the  $\text{h-RMnO}_3$  system.

## II. EXPERIMENTAL RESULTS

### A. Temperature- and field-dependent magnetization measurements

In order to clarify the spin structure in h-ErMnO<sub>3</sub> we scrutinized the magnetic phase diagram and extended it towards the milli-Kelvin regime to capture the actual ground state. Our magnetization measurements were performed at the LaMMB-MagLab of the Helmholtz-Zentrum Berlin using a h-ErMnO<sub>3</sub> single crystal of 20 mg grown by the floating-zone technique. For measurements above 1.8 K a standard vibrating sample magnetometer was used, whereas cantilever magnetometry was applied to study magnetic transitions below 1.8 K.

Figure 1(a) shows magnetization data for  $M(T)$  taken with increasing temperature  $dT/dt = +0.2$  K/min after field cooling ( $H \parallel c$ ). Note that identical curves were obtained for  $dT/dt < 0$  (not shown) indicating non-hysteretic behavior. For the remainder of this work we therefore restrict the discussion to measurements with  $dT/dt > 0$ .

As seen in Fig. 1(a), at 0.01 T a magnetic moment of  $4 \cdot 10^{-3}$  Am<sup>2</sup>/g is measured at 1.8 K. It decreases rapidly with increasing temperature showing a minimum in its derivative  $dM/dT$  around 2.2 K. The result is in agreement with earlier publications where the magnetization was attributed to long range magnetic order in the Er<sup>3+</sup> sublattice.<sup>15</sup> For increasing magnetic fields the associated change in  $M(T)$  becomes less pronounced and the minimum in  $dM/dT$  shifts to higher temperature (see gray triangles in Fig. 1(a)). The same trend is observed in magnetic torque measurements revealing a pronounced change in response between 1 K and 4 K (not shown). A second anomaly manifests at 0.75 T as a step-like increase in  $M(T)$ . This anomaly shifts continuously to higher temperatures when the magnetic field is increased further (see black circles in Fig. 1(a)). Figure 1(c) summarizes the results by showing the magnetic phase diagram in the temperature/magnetic-field plane. In order to trace the phase boundaries we investigated the magnetic-field dependence of the magnetization  $M(H)$  down to the milli-Kelvin range as exemplified by Fig. 1(b). All low-temperature magnetic-field scans clearly indicate two consecutive anomalies around 0.03 T and 0.6 T, respectively. Hence, based on our magnetization measurements we have to distinguish four different magnetically ordered states which are denoted as AFM, FIM<sub>1</sub>, FIM<sub>2</sub>, and FM in the phase diagram in Fig. 1(c).

The detailed analysis of the nature of these states, i.e. the corresponding spin structures and interactions, will be the topic of the following sections. We will distinguish four representations (magnetic space symmetries):  $\Gamma_1$  ( $P6_3cm$ ),  $\Gamma_2$  ( $P6_3\bar{c}m$ ),  $\Gamma_3$  ( $P6_3cm$ ), and  $\Gamma_4$  ( $P6_3\bar{c}m$ ). As we will see, lower symmetries like  $P6_3$  or  $P6_3\bar{c}$  do not have to be considered. For the sake of clarity we will first focus on the magnetic order of the Mn<sup>3+</sup> lattice, followed by a study of the Er<sup>3+</sup> order at the 4b and 2a sites. In the third part we will associate these spin structures to the magnetic phases identified in Fig. 1(c). An investigation of the intermediary transitions connecting the different magnetic phases follows. It will allow us to describe the sequence of magnetic phase transitions in a comprehensive

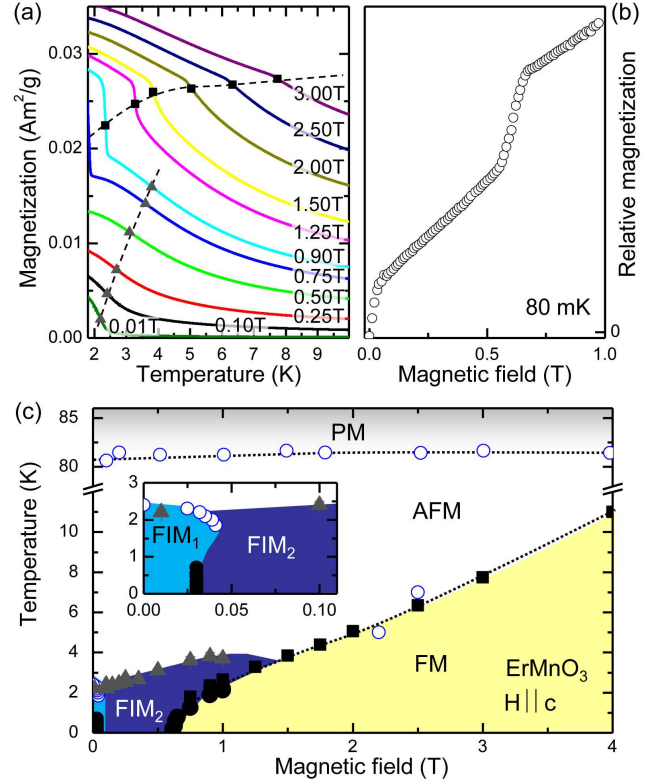


FIG. 1: (a) Temperature dependence of the magnetization  $M(T)$  in h-ErMnO<sub>3</sub> measured after field cooling. The data set, recorded with  $dT/dt = +0.2$  K/min in magnetic fields applied parallel to the  $c$ -axis, reveals two different anomalies indicated by gray triangles and black squares, respectively. As guide to the eye dashed lines indicate the magnetic-field dependence of the two transitions (b) Magnetic-field dependence of the magnetization  $M(H)$  at 80 mK. The curve shows two transitions that manifest as a step-like increase in  $M(H)$ . (c) HT-phase diagram of h-ErMnO<sub>3</sub>. Triangles and squares correspond to transitions deduced from  $M(T)$  (see (a)) while filled circles represent transitions observed in  $M(H)$ . Blue open circles are additional data points taken from Ref. 41.

model based on the coupling between the magnetic sublattices in the h-ErMnO<sub>3</sub> system with an outlook to the h-RMnO<sub>3</sub> system in general.

### B. SHG and neutron-diffraction study of the Mn<sup>3+</sup> spin structure

The magnetic Mn<sup>3+</sup> moments order antiferromagnetically at  $T_N \approx 80$  K.<sup>29</sup> The resulting structure has been discussed for more than five decades. Based on the extensive literature on h-ErMnO<sub>3</sub> the analysis and discussion can already be restricted to  $\Gamma_2^{\text{Mn}}$  and  $\Gamma_4^{\text{Mn}}$  as only possible magnetic representations for the Mn<sup>3+</sup> order (see Fig. 4 for a schematic illustration).<sup>30–33</sup> In order to scrutinize the emergence of the magnetic order according to either of these representations we performed complementary experiments by optical SHG and by neutron diffraction on selected site-specific reflec-

tions. The neutron-diffraction experiments were performed at the E2 beamline of the Helmholtz-Zentrum Berlin. A h-ErMnO<sub>3</sub> single crystal of  $2 \times 3 \times 5 \text{ mm}^3$  (180 mg) was cut from the same batch as the crystal studied by magnetometry. The sample was mounted in a <sup>3</sup>He/<sup>4</sup>He dilution insert and investigated in the  $h0l$  plane at a wavelength of 2.39 Å. Since neutron-diffraction experiments alone prohibit a unique distinction between the two aforementioned space groups,<sup>32</sup> SHG measurements were also conducted in order to uniquely determine the magnetic Mn<sup>3+</sup> order. SHG is described by the equation  $P_i(2\omega) = \epsilon_0 \chi_{ijk} E_j(\omega) E_k(\omega)$ . A light field  $\vec{E}$  at frequency  $\omega$  is incident onto a crystal, inducing a dipole oscillation  $\vec{P}(2\omega)$ , which acts as source of a frequency-doubled light wave. The susceptibility  $\chi_{ijk}$  couples incident light fields with polarizations  $j$  and  $k$  to a SHG contribution with polarization  $i$ . The magnetic and crystallographic symmetry of a compound is uniquely related to the set of nonzero components  $\chi_{ijk}$  and, therefore, allows to distinguish  $\Gamma_2^{\text{Mn}}$  and  $\Gamma_4^{\text{Mn}}$ .<sup>34</sup> Note that SHG has been applied earlier for investigating the magnetic structure of the Mn<sup>3+</sup> sublattice in h-ErMnO<sub>3</sub> but never before neutron diffraction and SHG were applied to the *same* sample and verified for the consistency of the two techniques.

Figure 2(a) shows a comparison of temperature-dependent neutron-diffraction and SHG intensities, the former for the (101) reflection and the latter for the  $\chi_{xxx}$  component of the nonlinear susceptibility tensor.<sup>30,32</sup> Both signals arise below  $T_N$  and exhibit the same temperature dependence emphasizing that SHG is coupling to the antiferromagnetic order of the Mn<sup>3+</sup> moments. The SHG measurement proves that the Mn<sup>3+</sup> moments of h-ErMnO<sub>3</sub> order according to the  $\Gamma_4^{\text{Mn}}$  representation in the temperature range  $10 \text{ K} < T < T_N$ , clearly discarding the  $\Gamma_2^{\text{Mn}}$  symmetry on the basis of selection rules: Only  $\Gamma_4^{\text{Mn}}$  allows SHG from  $\chi_{xxx}$  whereas  $\Gamma_2^{\text{Mn}}$  does not.<sup>34,35</sup>

Below about 2 K the SHG intensity from  $\chi_{xxx}$  begins to drop with time. According to Fig. 2(c) a decrease by 20% is obtained during the first 90 s after reducing the temperature from 5 to 1.8 K. The decrease slows down afterwards. Note that this behavior is reproducible and not caused by changes of the linear optical properties during cooling. A minuscule magnetic field accelerates the decrease of the SHG signal. Figure 2(d) shows that it steadily drops to zero within 30 s when a magnetic field is ramped from 0 to 0.05 T linearly with time. The gradual decrease of the  $\chi_{xxx}$  component from its full value to zero is characteristic for a  $\Gamma_4^{\text{Mn}} \rightarrow \Gamma_2^{\text{Mn}}$  transition of the Mn<sup>3+</sup> sublattice.<sup>18,30,36,37</sup> This is contrasted by only a minor dip in the neutron diffraction at the (101) peak between 1 K and 4 K. The persistence of the (101) reflection is expected as  $\Gamma_4^{\text{Mn}}$  and  $\Gamma_2^{\text{Mn}}$  representations lead to (101) peak intensities differing by only 7% (see also Fig. 2(b)).<sup>32,33</sup> The dip emerging at the intermediary transition, however, cannot be explained on the basis of symmetry.

We therefore verified its occurrence by repeating the temperature dependent measurement on a second magnetic reflection coupling to the Mn<sup>3+</sup> order. For this purpose we chose the (103) reflection as SIMREF2.6 simulations<sup>40</sup> (see Fig. 2(f)) reveal no intermixing with Er<sup>3+</sup> contributions.<sup>38</sup> Figure 2(e) shows a dip between 1 K and 4 K that is even more pronounced compared to the one seen in Fig. 2(a). It points to a

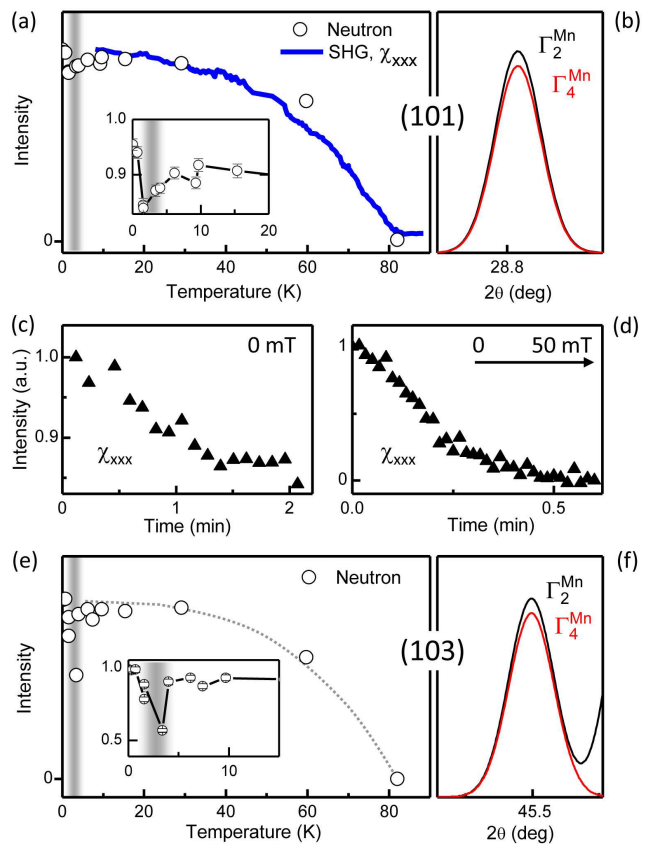


FIG. 2: (a) Comparison of optical SHG measurements and neutron-diffraction experiments. Both the  $\chi_{xxx}$  component of the nonlinear susceptibility tensor and the magnetic (101) reflection arise at  $T_N = 80 \text{ K}$ . Between 1 K and 4 K the (101) peak intensity displays a dip which is shown in detail in the inset to Fig. 2(a). (b) SIMREF2.6 simulation of the relative (101) peak intensity assuming Mn<sup>3+</sup> order according to  $\Gamma_2^{\text{Mn}}$  and  $\Gamma_4^{\text{Mn}}$ . (c), (d) Time dependence of the SHG signal from  $\chi_{xxx}$  after decreasing the temperature from 5 to 1.8 K. The steady gradual decrease observed in (c) is supported by a minuscule magnetic field  $H \parallel c$  ramped from 0 to 0.05 T linearly with time in (d). (e) Temperature dependence of the (103) reflection probing the Mn<sup>3+</sup> order as corroborated by the simulations presented in (f). The gray dotted line retraces the SHG data shown in (a) serving as guide to the eye. In agreement with (a) the (103) peak intensity transiently breaks down between 1 K and 4 K.

transient breakdown of the Mn<sup>3+</sup> order that will be discussed in Section III. Note that the dip in the Mn<sup>3+</sup>-related intensity was not observed in earlier neutron measurements on the same sample where the base temperature of the experiment was limited to 1.8 K.<sup>39</sup> This emphasizes the importance of establishing a well-defined ground state, here by entering the milli-Kelvin regime, for performing an accurate analysis of the magnetic order in this strongly frustrated system.

### C. Neutron-diffraction study of the Er<sup>3+</sup> spin structure

Analogous to the case of the Mn<sup>3+</sup> moments four different representations denoted  $\Gamma_1^{\text{Er}}$  to  $\Gamma_4^{\text{Er}}$  have to be distinguished

for the  $\text{Er}^{3+}$  order.<sup>12,26–28</sup> However, in contrast to the  $\text{Mn}^{3+}$  lattice no SHG contributions coupling to the rare-earth system were found so that our symmetry analysis is entirely based on neutron data.

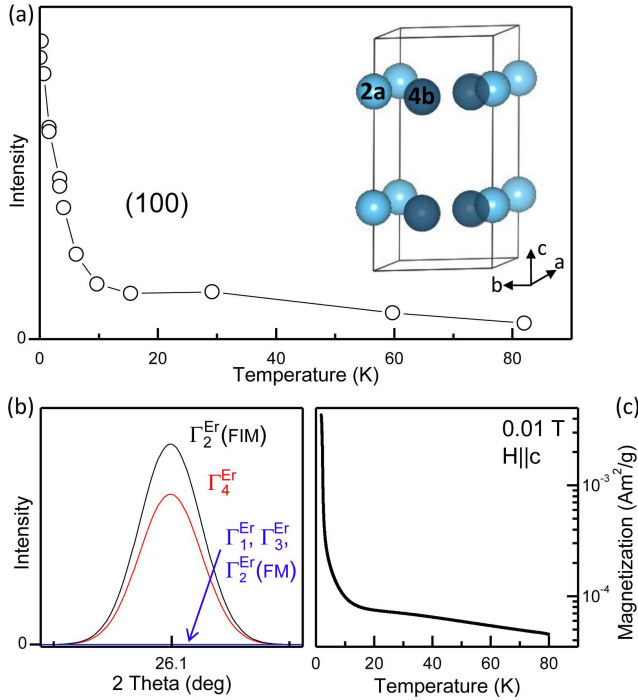


FIG. 3: (a) Temperature dependence of the (100) peak intensity and schematic illustration of the  $\text{Er}^{3+}(2a)$  and  $\text{Er}^{3+}(4b)$  positions in the hexagonal unit cell of h- $\text{ErMnO}_3$ . (b) SIMREF2.6 simulation reveal that a (100) reflection can emerge only for  $\text{Er}^{3+}$  order according to the  $\Gamma_4^{\text{Er}}$  or  $\Gamma_2^{\text{Er}}(\text{FIM})$  representation with the latter one leading to the stronger reflection. (c)  $M(T)$  measurement taken at 10 mT exhibiting a similar temperature dependence as the (100) peak intensity.

In Fig. 3(a) we present the temperature dependence of the (100) reflection of h- $\text{ErMnO}_3$ . Since neither  $\Gamma_4^{\text{Mn}}$  order nor  $\Gamma_2^{\text{Mn}}$  order allows  $\text{Mn}^{3+}$  contributions to the (100) peak, any contribution to this peak has to be attributed to the magnetic order of the  $\text{Er}^{3+}$  moments.<sup>18</sup> The (100) peak emerges at 80 K. Its intensity increases monotonously with decreasing temperature down to about 10 K where a change of slope occurs. Thus, according to Fig. 3(a) the  $\text{Er}^{3+}$  sublattice does not order at 3 K as reported before,<sup>15</sup> but already at  $T_N$ . Yet, the temperature dependence of the  $\text{Er}^{3+}$ -related signal is different from those related to  $\text{Mn}^{3+}$  in Fig. 2. This is reminiscent of the situation in h- $\text{DyMnO}_3$  and h- $\text{YbMnO}_3$  and indicates that the magnetic  $\text{Er}^{3+}$  order is related to the antiferromagnetic  $\text{Mn}^{3+}$  order by the magnetic triggering mechanism identified in Ref. 18. The triggering mechanism describes a biquadratic order-parameter coupling between two subsystems of a compound. Ordering in one of them can induce ordering in the other at the same temperature whenever the associated coupling term lowers the ground state energy.<sup>45</sup> Because of the biquadratic nature of the coupling the  $\text{Er}^{3+}$  and  $\text{Mn}^{3+}$  sublattices can order according to different magnetic space groups at  $T_N$ . Thus, in spite of the known magnetic order of the  $\text{Mn}^{3+}$

system, the magnetic  $\text{Er}^{3+}$  system may order according to any of the four representations  $\Gamma_1^{\text{Er}}$  to  $\Gamma_4^{\text{Er}}$ .

Supplementary simulations by SIMREF2.6, however, reveal that for  $\text{Mn}^{3+}$  order according to  $\Gamma_{2,4}^{\text{Mn}}$  the experimentally observed (100) reflection only arises if the  $\text{Er}^{3+}$  sublattice orders according to the  $\Gamma_2^{\text{Er}}$  or  $\Gamma_4^{\text{Er}}$  representation. In turn it is forbidden for  $\Gamma_1^{\text{Er}}$  and  $\Gamma_3^{\text{Er}}$  as shown by the simulations in Fig. 3(b). We further note that  $\Gamma_2^{\text{Er}}$  involves ferromagnetic order on the 2a and 4b sites and is therefore associated to a macroscopic magnetization which can be excluded for temperatures between 10 K and  $T_N$  based on the magnetization measurement in Fig. 3(c). We therefore conclude “compatible” magnetic order of the  $\text{Er}^{3+}$  and  $\text{Mn}^{3+}$  sublattices according to the same representation,  $\Gamma_4^{\text{Er,Mn}}$ , at  $T_N$  with an antiferromagnetically ordered  $\text{Er}^{3+}(4b)$  site and a disordered  $\text{Er}^{3+}(2a)$  site as sketched in Fig. 4 (AFM-phase). This is qualitatively the same scenario met in h- $\text{YbMnO}_3$ ,<sup>12</sup> but different from h- $\text{DyMnO}_3$ ,<sup>18</sup> and h- $\text{HoMnO}_3$ .<sup>9,43</sup>

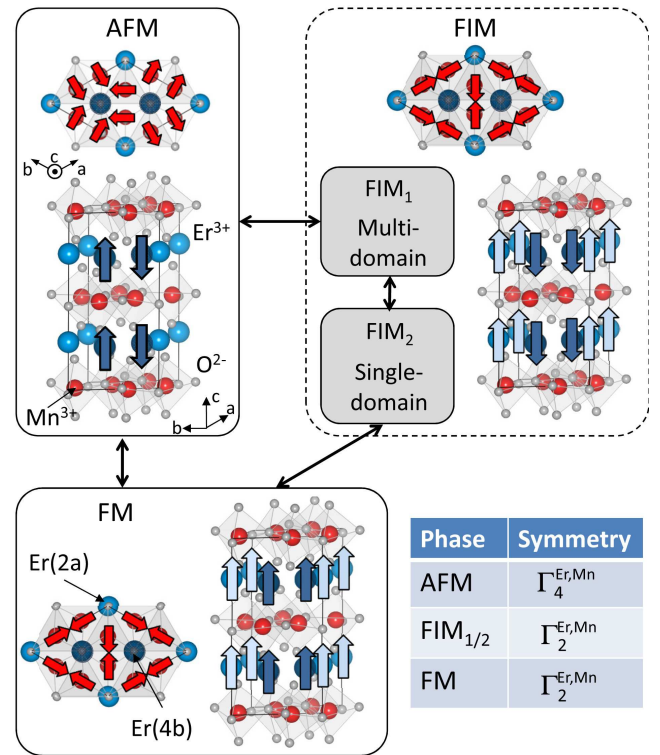


FIG. 4: Schematic illustration of the spin structure in the different magnetically ordered phases of h- $\text{ErMnO}_3$ . Three phases have to be distinguished: The antiferromagnetic (AFM) phase, the ferromagnetic (FIM) phase (magnetic ground state), and the magnetic-field-induced ferromagnetic (FM) phase. Note that depending on the strength of the magnetic-field  $H||c$  the crystal can either be in a single-domain (FIM<sub>2</sub>) or a multi-domain (FIM<sub>1</sub>) state in the FIM phase. Black arrows between the different phases indicate possible temperature / magnetic-field driven transitions.

Below 10 K the pronounced increase of the (100) peak intensity indicates a change in the magnetic  $\text{Er}^{3+}$  order. This change is matched by the increase in  $M(T)$  seen in Fig. 3(c).

The only possible transition that is in accordance with the neutron-diffraction and the magnetization measurements is a  $\Gamma_4^{\text{Er}} \rightarrow \Gamma_2^{\text{Er}}$  transition of the  $\text{Er}^{3+}$  sublattices. First of all, as mentioned before, the (100) reflection exclusively occurs for the representations  $\Gamma_2^{\text{Er}}$  and  $\Gamma_4^{\text{Er}}$ . Regarding the two remaining representations only  $\Gamma_2^{\text{Er}}$  allows for the magnetization observed at low temperature. This narrows the number of possible magnetic structures down to two, having either an antiparallel ( $\Gamma_2^{\text{Er}}$ (FIM)) or parallel ( $\Gamma_2^{\text{Er}}$ (FM)) alignment of the  $\text{Er}^{3+}$  moments on the 4b and 2a sites. The SIMREF2.6 simulations summarized in Fig. 3(b), however, clearly discard  $\text{Er}^{3+}$  order according to  $\Gamma_2^{\text{Er}}$ (FM) because in this case destructive interference of the  $\text{Er}^{3+}$ (4b) and  $\text{Er}^{3+}$ (2a) contributions suppress the (100) reflection. In contrast, constructive interference occurs for an antiparallel orientation of the  $\text{Er}^{3+}$ (4b) and  $\text{Er}^{3+}$ (2a) spins and explains the drastic increase of the (100) peak intensity seen in Fig. 3(a). We thus conclude that the ground state of the  $\text{Er}^{3+}$  order is ferrimagnetic,  $\Gamma_2^{\text{Er}}$ (FIM), with antiparallel orientation of the  $\text{Er}^{3+}$  moments on the 4b sites relative to the 2a sites (FIM-phase in Fig. 4). In terms of representations, the magnetic order of h-ErMnO<sub>3</sub> at low temperature is again the same as in h-YbMnO<sub>3</sub><sup>12</sup> and different from h-DyMnO<sub>3</sub>,<sup>18</sup> and h-HoMnO<sub>3</sub>.<sup>9,43</sup>

#### D. Microscopic magnetic structure of the $\text{Er}^{3+}$ and $\text{Mn}^{3+}$ sublattices

Based on the magnetization, SHG, and neutron-diffraction experiments we can now derive a coherent model describing the different magnetic states indicated in the phase diagram in Fig. 1(c). We have already seen that the  $\text{Mn}^{3+}$  moments and the  $\text{Er}^{3+}$  moments on the 4b sites order antiferromagnetically in the AFM-phase while the  $\text{Er}^{3+}$ (2a) spins remain disordered. The order corresponds to the  $\Gamma_4^{\text{Er,Mn}}$  representation and is schematically depicted in Fig. 4. The FIM<sub>1</sub> phase encountered toward 0 K in zero magnetic field is characterized by antiferromagnetic  $\text{Mn}^{3+}$  order and ferrimagnetic  $\text{Er}^{3+}$  order, both according to the  $\Gamma_2^{\text{Er,Mn}}$  representation.

Additional information on the nature of this phase can be extracted from the  $M(H)$  measurement presented in Fig. 1(b). The pronounced response to small magnetic fields ( $H \lesssim 0.03$  T) points to the formation of a ferrimagnetic multi-domain state in zero magnetic field with an 1 : 1 ratio of domains with  $+M_z$  and  $-M_z$ . Consequently, the FIM<sub>2</sub> phase denotes the ferrimagnetic single-domain state with a coercive field of  $\approx 0.03$  T toward 0 K as boundary between the FIM<sub>1</sub> and FIM<sub>2</sub> states. The ferrimagnetic nature of this state is further reflected by the change in signal occurring at the FIM<sub>2</sub>  $\rightarrow$  FM transition in Fig. 1(b). By linearly extrapolating the  $M(H)$  data gained within the two phases and comparing the corresponding  $M(0)$  values we find that the magnetization almost triples across the transition. This behavior can be understood in terms of a change from an antiparallel to a parallel arrangement of the  $\text{Er}^{3+}$ (4b) spins with respect to the  $\text{Er}^{3+}$ (2a) spins, i.e., a change of the magnetic moment per unit cell from  $(4-2) \cdot \mu_{\text{Er}^{3+}}$  to  $(4+2) \cdot \mu_{\text{Er}^{3+}}$ . The transition to the ferromagnetic  $\text{Er}^{3+}$  order does not involve a change of magnetic symmetry

and is therefore still described by the  $\Gamma_2^{\text{Er,Mn}}$  representation.

Note that earlier studies did not distinguish between the FIM<sub>1</sub> and FIM<sub>2</sub> region of the ferrimagnetic phase. In contrast, the ferrimagnetic rare-earth order was believed to be suppressed by small magnetic-fields of only 0.05 T which would misleadingly imply weak exchange between the  $\text{Er}^{3+}$  spins.<sup>41</sup>

After the unique determination of the microscopic magnetic structure of h-ErMnO<sub>3</sub> we can now turn to the intermediary states encountered during the transitions between the AFM, FIM, and FM phases. These transitions will allow us to draw further conclusions about the coupling between the  $4f$  moments at the  $\text{Er}^{3+}$ (2a) and  $\text{Er}^{3+}$ (4b) sites and the  $3d$  moments of  $\text{Mn}^{3+}$ .

#### E. Magnetic interaction of the $\text{Er}^{3+}$ and $\text{Mn}^{3+}$ sublattices

The comparison of Figs. 2 and 3(a) already revealed an interaction between the  $\text{Mn}^{3+}$  and  $\text{Er}^{3+}$ (4b) sublattices: The former triggers the order in the latter at  $T_N$ . Below 10 K the  $\text{Er}^{3+}$ (2a) order supplements the  $\text{Er}^{3+}$ (4b) order and additional transitions occur as seen in the phase diagram in Fig. 1(c). Figure 3(a) reveals that, unlike the  $\text{Er}^{3+}$ (4b) order, the  $\text{Er}^{3+}$ (2a) is not triggered by the  $\text{Mn}^{3+}$  order. The  $\text{Er}^{3+}$  spins at the 2a sites begin to order at higher temperature ( $\sim 10$  K) compared to the observed reorientation of the  $\text{Mn}^{3+}$  spins ( $\sim 2$  K). This precludes the triggering mechanism as it would require identical reorientation temperatures for the two sublattices.

Hence, we propose that here the  $\text{Er}^{3+}$ (2a) order drives the reordering of the  $\text{Mn}^{3+}$  sublattice through non-biquadratic triggered (and thus linear) order-parameter coupling. This assumption is supported by three observations: (i) The magnetic rare-earth order continues to strengthen toward lower temperature whereas the  $\text{Mn}^{3+}$  order is already saturated. Therefore the  $\text{Mn}^{3+}$  order cannot be responsible for the  $\text{Er}^{3+}$ (2a) order. (ii) The reordering of the  $\text{Mn}^{3+}$  sublattice “follows” the  $\text{Er}^{3+}$ (2a) order at lower temperature. Therefore the latter order, which is continuously strengthening with decreasing temperature, must be guiding the reorientation. (iii) The  $\text{Mn}^{3+}$  sublattice adopts the emerging  $\Gamma_2$ -like order of the  $\text{Er}^{3+}$ (2a) sublattice by undergoing a  $\Gamma_4^{\text{Mn}} \rightarrow \Gamma_2^{\text{Mn}}$  transition.

The data shown so far do not reveal the role of the  $\text{Er}^{3+}$ (4b) in this interaction: Once the 2a site orders it dominates the (100) reflection in Fig. 3(a) to an extent that the response from the  $\text{Er}^{3+}$ (4b) site is obscured. We therefore investigated various  $h0l$  diffraction peaks by SIMREF2.6 simulation in order to identify other magnetic peaks with a similar weight of contributions from the  $\text{Mn}^{3+}$ , the  $\text{Er}^{3+}$ (2a), and the  $\text{Er}^{3+}$ (4b) that would allow us to analyzing the interplay between  $\text{Er}^{3+}$  moments on the 2a and 4b sites. As revealed by Fig. 5(b), the (102) reflection fulfills this condition. We find that the intensity of the (102) reflection experiences striking breakdowns around 2.5 K and 7 K revealing magnetic reorientations with a transient breakdown of the magnetic order at these temperatures.<sup>42,44</sup> The breakdown at 2.5 K is related to the  $\text{Mn}^{3+}$  sublattice because it is also observed in the (101) and

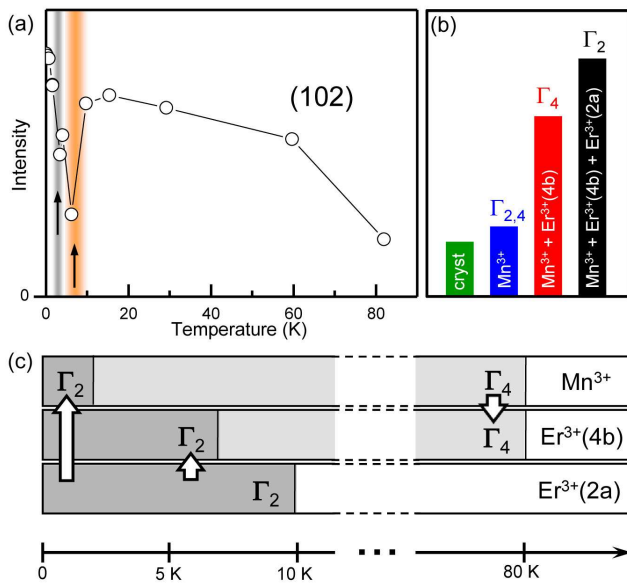


FIG. 5: (a) Temperature dependence of the (102) reflection. An increase in intensity occurs below  $T_N = 80$  K with consecutive breakdowns below 10 K. (b) Decomposition of contributions to the (102) peak intensity based on SIMREF2.6 simulations. Below  $T_N$  the crystallographic contribution (cryst) to the (102) reflection is supplemented by magnetic contributions originating from  $\text{Mn}^{3+}$  and  $\text{Er}^{3+}$ . (c) Sketch illustrating the mutual induction of the magnetic 3d and 4f order. Below  $T_N$  the  $\text{Mn}^{3+}$  order triggers magnetic long range order on the 4b sites as indicated by the white arrow. In contrast, magnetic moments on the 2a sites only order below 10 K inducing a reorientation of  $\text{Er}^{3+}(4b)$  moments which is followed by a reorientation of the  $\text{Mn}^{3+}$  spins.

(103) reflexes (see Fig. 2) which are entirely determined by the  $\text{Mn}^{3+}$  order. In turn, the additional breakdown at 7 K can only indicate a magnetic reorientation of the  $\text{Er}^{3+}(4b)$  sublattice. We conclude that, like the  $\text{Mn}^{3+}$  order, the  $\text{Er}^{3+}(4b)$  order toward 0 K is driven by the  $\text{Er}^{3+}(2a)$  order because it follows the same criteria (i-iii) as the  $\text{Mn}^{3+}$  reordering.

In summary, toward 0 K h- $\text{ErMnO}_3$  undergoes a transformation with a change of the representation according to  $\Gamma_4^{\text{Er,Mn}} \rightarrow \Gamma_2^{\text{Er,Mn}}$ . However, the  $\Gamma_2$  phase is assumed at a different temperature for the  $\text{Er}^{3+}(2a)$ , the  $\text{Er}^{3+}(4b)$ , and the  $\text{Mn}^{3+}$  sublattices.

### III. COMPREHENSIVE MODEL FOR THE MAGNETIC PHASE TRANSITIONS OF HEXAGONAL $\text{ErMnO}_3$

By combining the analysis of the magnetic phase diagram in Sections II A to II D and the analysis of the magnetic transitions between these phases in Section II E we are now able to present a comprehensive scenario of the magnetic interactions and the resulting phase transitions in h- $\text{ErMnO}_3$  with a projection on the h- $\text{RMnO}_3$  series as a whole. We distinguish two fundamentally different temperature ranges as illustrated in Fig. 5(c):

*Between the Néel temperature and  $\sim 10$  K:* In this range

the magnetic structure is determined by the ordering of the  $\text{Mn}^{3+}$  sublattice. The  $\text{Mn}^{3+}$  spins order antiferromagnetically at  $T_N$  and promote rare-earth ordering on the  $\text{Er}^{3+}(4b)$  site. The  $\text{Er}^{3+}(4b)$  order is induced at the same temperature,  $T_N$ , via a triggering mechanism with biquadratic  $\text{Mn}^{3+}-\text{Er}^{3+}(4b)$  order-parameter coupling. Both the  $\text{Mn}^{3+}$  and  $\text{Er}^{3+}(4b)$  lattice order according to the same representation,  $\Gamma_4^{\text{Er,Mn}}$ . However, because of the biquadratic coupling this compatibility is not mandatory. Indeed,  $\text{Mn}^{3+}$  and  $\text{Er}^{3+}(4b)$  order according to different representations in h- $\text{DyMnO}_3$ . In any case, the  $\text{Er}^{3+}(2a)$  site remains disordered in this temperature range.

*Below  $\sim 10$  K:* In this range the magnetic structure is determined by the ordering of the  $\text{Er}^{3+}(2a)$  sublattice. The spins arrange uniformly at  $\sim 10$  K according to the representation  $\Gamma_2^{\text{Er}}$  with a macroscopic magnetization per domain and a nonzero net magnetization once the magnetic field lifts the degeneracy between oppositely oriented FIM domain states. When the  $\text{Er}^{3+}(2a)$  order strengthens toward low temperature, the  $\text{Er}^{3+}(2a)$  ordering at first induces  $\Gamma_4^{\text{Er}} \rightarrow \Gamma_2^{\text{Er}}$  reordering on the  $\text{Er}^{3+}(4b)$  site ( $\sim 7$  K) followed by  $\Gamma_4^{\text{Mn}} \rightarrow \Gamma_2^{\text{Mn}}$  reordering of the  $\text{Mn}^{3+}$  sublattice ( $\sim 2.5$  K). The coupling to the  $\text{Er}^{3+}(2a)$  sublattice is linear and therefore not guided by the triggering mechanism. This is evidenced by the difference between the (re-) ordering temperatures and the accordance of the representations describing the magnetic order in the different sublattices. The  $\text{Er}^{3+}(2a)$  and  $\text{Er}^{3+}(4b)$  sites maintain an antiparallel spin orientation that can be overcome in an external magnetic field in the order of magnitude of 1 T driving a transition from ferrimagnetic to ferromagnetic  $\text{Er}^{3+}$  order. A similar situation is met in all rare-earth h- $\text{RMnO}_3$  compounds except in h- $\text{HoMnO}_3$  where the  $\text{Ho}^{3+}$  ground state is antiferromagnetic, yet with similar sublattice correlations as in the other h- $\text{RMnO}_3$  compounds.

### IV. SUMMARY

In conclusion, the combination of magnetization, SHG, and neutron-diffraction experiments at temperatures down to the milli-Kelvin regime reveals important features in the magnetic phase diagram of h- $\text{ErMnO}_3$ . We identify the spin structure in the respective magnetic phases, the magnetic coupling between the  $\text{Mn}^{3+}$ ,  $\text{Er}^{3+}(4b)$ , and  $\text{Er}^{3+}(2a)$  sublattices, and the resulting phase transitions establishing the phase diagram. We find a high-temperature range above 10 K where the  $\text{Mn}^{3+}$  sublattice induces magnetic  $\text{Er}^{3+}$  order and a low-temperature range below 10 K where the  $\text{Er}^{3+}$  sublattice induces magnetic  $\text{Mn}^{3+}$  order. Most of all, we find that the ordering on the 4b and 2a sites of the  $\text{Er}^{3+}$  sublattices play a strikingly independent and different role in establishing the magnetic order in h- $\text{ErMnO}_3$ . The comprehensive model for the phase diagram of the h- $\text{ErMnO}_3$  developed in this work can be projected onto the other rare-earth h- $\text{RMnO}_3$  compounds with only small variations. Thus, we are now able to understand the complex magnetic phases of the h- $\text{RMnO}_3$  system on a universal basis.

D.M. acknowledges support by the Alexander von Humboldt Foundation and the NSF Science and Technology Center

(E3S). M.F. thanks the DFG (SFB 608) for subsidy.

- \* Email address: meier@berkeley.edu
- 2 T. Kimura, T. Goto, H. Shintani, K. Ishizaka, T. Arima, and Y. Tokura, *Nature* **426**, 55 (2003).
  - 3 N. Hur, S. Park, P. A. Sharma, J. S. Ahn, S. Guha, and S.-W. Cheong, *Nature* **429**, 392 (2004).
  - 4 M. Fiebig, *J. Phys. D* **38**, 123 (2005).
  - 5 S.-W. Cheong and M. Mostovoy, *Nat. Mater.* **6**, 13 (2007).
  - 6 Ph. Coeuré, P. Guinet, J. C. Peuzin, G. Buisson, and E. F. Bertaut, *Proc. Int. Meet. Ferroelectr.* **1**, 332 (1966).
  - 7 R. Pauthenet and C. Veyret, *J. Phys. (Paris)* **31**, 65 (1970). (Curie temperatures are incorrectly listed due to a misprint.)
  - 8 Y. Kumagai, A. A. Belik, M. Lilienblum, N. Leo, M. Fiebig, and N. A. Spaldin, *Phys. Rev. B* **85**, 174422 (2012).
  - 9 Th. Lottermoser, Th. Lonkai, U. Amann, D. Hohlwein, J. Ihringer, and M. Fiebig, *Nature* **430**, 541 (2004).
  - 10 S. Lee, A. Pirogov, M. Kang, K.-H. Jang, M. Yonemura, T. Kamiyama, S.-W. Cheong, F. Gozzo, N. Shin, H. Kimura, Y. Noda, and J.-G. Park, *Nature* **451** 805 (2008).
  - 11 M. Fiebig, Th. Lottermoser, D. Fröhlich, A. V. Goltsev, and R. V. Pisarev, *Nature* **419** 818 (2002).
  - 12 X. Fabrèges, I. Mirebeau, P. Bonville, S. Petit, G. Lebras-Jasmin, A. Forget, G. André, and S. Pailhès, *Phys. Rev. B* **78**, 214422 (2008).
  - 13 S. Harikrishnan, S. Rößler, C. N. Naveen Kumar, H. L. Bhat, U. K. Rößler, S. Wirth, F. Steglich, and S. Elizabeth, *J. Phys.: Condens. Matter* **21**, 096002 (2009).
  - 14 Th. Lonkai, D. Hohlwein, J. Ihringer, and W. Prandl, *Appl. Phys. A*, **74**, S843 (2002).
  - 15 H. Sugie, N. Iwata, and K. Kohn, *J. Phys. Soc. Jpn.* **71**, 1558 (2002).
  - 16 I. Munawar and S. H. Curnoe, *J. Phys.: Condens. Matter* **18**, 9575 (2006).
  - 17 T. A. Tyson, T. Wu, K. H. Ahn, S.-B. Kim, and S.-W. Cheong, *Phys. Rev. B* **81**, 054101 (2010).
  - 18 Ch. Wehrenfennig, D. Meier, Th. Lottermoser, Th. Lonkai, J.-U. Hoffmann, N. Aliouane, D. N. Argyriou, and M. Fiebig, *Phys. Rev. B* **82**, 100414(R) (2010).
  - 19 D. Meier, S. Seidel, A. Cano, K. Delaney, Y. Kumagai, M. Mostovoy, N. A. Spaldin, R. Ramesh, and M. Fiebig, *Nature Mat.* **11**, 284 (2012).
  - 20 D. Meier, M. Lilienblum, P. Becker, L. Bohatý, N. A. Spaldin, R. Ramesh, and M. Fiebig, *Phase Transit.*, DOI:10.1080/01411594.2012.696116 (2012).
  - 21 Weida Wu, Y. Horibe, N. Lee, S.-W. Cheong, and J. R. Guest, *Phys. Rev. Lett.* **108**, 077203 (2012).
  - 22 Y. Du, X. L. Wang, D. P. Chen, S. X. Dou, Z. X. Cheng, M. Higgins, G. Wallace, and J. Y. Wang, *Appl. Phys. Lett.* **99**, 252107 (2011).
  - 23 Y. Geng, N. Lee, Y. J. Choi, S.-W. Cheong, and W. Wu, arXiv:1201.0694.
  - 24 N. Iwata and K. Kohn, *Ferroelectrics* **219**, 161 (1998); *J. Phys. Soc. Jap.* **67** 3318 (1998). (The results for ErMnO<sub>3</sub> and HoMnO<sub>3</sub> have to be exchanged.)
  - 25 D. B. Litvin, *Acta Cryst.* **A57**, 729 (2001).
  - 26 A. Muñoz, J. A. Alonso, M. J. Martínez-Lope, M. T. Casáis, J. L. Martínez, and M. T. Fernández-Díaz, *Phys. Rev. B* **62**, 9498 (2000).
  - 27 S. Nandi, A. Kreyssi, J. Q. Yan, M. D. Vannette, J. C. Lang, L. Tan, J. W. Kim, R. Prozorov, T. A. Lograsso, R. J. McQueeney, and A. I. Goldman, *Phys. Rev. B* **78**, 075118 (2008).
  - 28 M. Fiebig, Th. Lottermoser, and R. V. Pisarev, *J. Appl. Phys.* **93**, 8194 (2003).
  - 29 W. C. Koehler, H. L. Yakel, E. O. Wollan, and J. W. Cable, *Phys. Lett.* **9**, 93 (1964).
  - 30 M. Fiebig, C. Degenhardt, and R. V. Pisarev, *Phys. Rev. Lett.* **88**, 027203 (2002).
  - 31 M. C. Sekhar, S. Lee, G. Choi, C. Lee, and J.-G. Park, *Phys. Rev. B* **72**, 014402 (2005).
  - 32 J. Park, U. Kong, S.I. Choi, J.-G. Park, C. Lee, and W. Jo, *Appl. Phys. A* **74**, 802 (2002).
  - 33 S. Lee, and J.-G. Park, *Neutron News* **17** 24, (2006).
  - 34 M. Fiebig, V. V. Pavlov, and R. V. Pisarev, *J. Opt. Soc. Am. B* **22**, 96 (2005).
  - 35 T. Kordel, C. Wehrenfennig, D. Meier, Th. Lottermoser, and M. Fiebig, *Phys. Rev. B* **80**, 045409 (2009)
  - 36 M. Fiebig, D. Fröhlich, K. Kohn, St. Leute, Th. Lottermoser, V. V. Pavlov, and R.V. Pisarev, *Phys. Rev. Lett.* **84**, 5620 (2000).
  - 37 M. Fiebig, T. Lottermoser, T. Lonkai, A. Goltsev, and R. Pisarev, *J. Magn. Magn. Mater.* **290-291**, 883 (2005).
  - 38 Based on Section II C the SIMREF2.6 simulation was performed assuming Er<sup>3+</sup> order according to the  $\Gamma_2^{\text{Er}}$  and  $\Gamma_4^{\text{Er}}$  representation.
  - 39 D. G. Tomuta, PhD thesis (2003), Leiden University, The Netherlands.
  - 40 H. Ritter, J. Ihringer, J. K. Maichle, W. Prandl, SimRef2.6 (1999), <http://www.uni-tuebingen.de/uni/pki/simref/simref.html>.
  - 41 F. Yen, C. R. dela Cruz, B. Lorenz, E. Galstyan, Y. Y. Sun, M. M. Gospodinov, and C. W. Chu, *J. Mater. Res.* **22**, 2163 (2007).
  - 42 Th. Lonkai, PhD thesis (2004), Eberhard-Karls-Universität Tübingen, Germany.
  - 43 O. P. Vajk, M. Kenzelmann, J. W. Lynn, S. B. Kim, and S.-W. Cheong, *Phys. Rev. Lett.* **94**, 087601 (2005).
  - 44 J. S. Helton, D. K. Singh, H. S. Nair, and S. Elizabeth, *Phys. Rev. B* **84**, 064434 (2011).
  - 45 J. Holakowský, *phys. stat. sol. (b)* **56**, 615 (1973).